IX International Conference on Computational Methods for Coupled Problems in Science and Engineering
COUPLED PROBLEMS 2021
E. Oñate, M. Papadrakakis and B. Schrefler (Eds)

A DETERMINISTIC APPROACH FOR SHAPE AND TOPOLOGY OPTIMISATION UNDER MATERIAL UNCERTAINTY IN ADDITIVE MANUFACTURING

CHETRA MANG*, LIONEL ZOGHAIB , JULIEN CORTIAL†**
CHIARA NARDONI*, DAVID DANAN* , FELIPE BORDEU†

*Institut de Recherche Technologique SystemX
Btiment 660, Rue Noetzlin 91191 Gif-sur-Yvette
e-mail: chetra.mang@irt-systemx.fr
e-mail: chiara.nardoni@irt-systemx.fr
e-mail: david.danan@irt-systemx.fr
**Airbus CRT
22 Rue du Gouverneur Général Eboué, 92130 Issy-Les-Moulineaux
e-mail: lionel.zoghaib@airbus.com
†Safran Tech, , Digital Sciences & Technologies
Rue des Jeunes Bois, Châteaufort, CS-80112-78777 Magny-les-Hameaux, France
e-mail: julien.cortial@safrangroup.com
e-mail: felipe.bordeu@safrangroup.com

Key words: Additive manufacturing, topology optimisation, deterministic approach, material uncertainty

Abstract. The present work aims at handling uncertain materials in shape and topology optimisation applied to additive manufacturing. More specifically, we minimise an objective function combining the mean values of standard cost functions and assume that the uncertainties are small and generated by two random variables. These two variables representing the amplitude of the Young's modulus correspond to the zone of porosity inclusion and surface roughness defects. A deterministic approach that relies on a second-order Taylor expansion of the cost function has been proposed by Allaire & Dapogny [2]. The present work proposes a general framework to handle uncertainties of the Young's modulus in which its amplitude is divided into N zones and then applied onto two zones corresponding to the porosity inclusion and surface roughness defects. We demonstrate the effectiveness of the approach in the context of the level-set-based topology optimisation for the robust compliance minimisation of three-dimensional cantilever test cases.

1 INTRODUCTION

Additive manufacturing (AM) technology has demonstrated its effectiveness in producing complex part designs. However, it is well known that AM leads to high uncertainties at the microstructure level that affect the suitability of the part as-built [4]. These uncertainties are linked to geometric defects such as porosity and surface roughness which directly result in high variability of material properties such as the Young's modulus [1]. The present paper aims at handling material uncertainty in the context of shape and topology optimisation for additive manufacturing. Concretely, we minimise a composite objective function depending on the mean values of standard cost functions and assume that the uncertainties are small and generated by a finite number of random variables. More precisely, two random variables represent the porosity and the surface roughness uncertainties characterised by variations of the Young's modulus. A deterministic approach that relies on a second-order Taylor expansion of the cost function has been proposed by Allaire and Dapogny [2]. We demonstrate the effectiveness of the approach in the context of the level-set-based topology optimisation for the robust compliance minimisation on three-dimensional test cases. From a computational point of view, our strategy relies on a body-fitted mesh evolution approach allowing to generate adapted, high quality meshes of the mechanical parts at each stage of the optimisation process [3].

2 Young's modulus characterisation

Metal bed powder based additive manufacturing such as selective laser melting (SLM) has shown its success in manufacturing parts from a metalic material. Even though the SLM technology has made significant progress, defects such as porosity inclusion and surface roughness are still present [6]. These defects have a direct influence on mechanical properties such as the Young's modulus [7]. This section introduces how to characterise the Young's modulus based on the porosity inclusion and surface roughness defects produced by the SLM additive manufacturing process.

The equivalent Young's modulus of a porous material can be defined by the exponential law as follows [5]:

$$E = E_0(1 - \frac{p}{p_c})^f, \tag{1}$$

where E_0 is the Young's modulus of the solid material, p is the porosity of the porous material, p_c is the nominal porosity for which the effective Young's modulus E is zero, and f is a constant depending on the morphology and geometry of the grain composing the porous material.

The defects produced by the additive manufacturing are characterised by the equivalent bi-material comprising an interior material (blue) and an exterior material (red) as shown in Figure 1 on the right. The interior material corresponds to the porosity inclusion defect. The exterior material corresponds to the surface roughness defect. The exterior material is characterised by the volume generated by the mean surface of the surface roughness

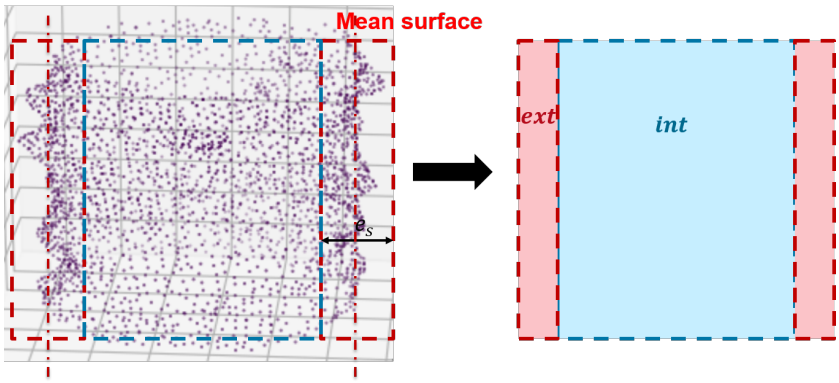

Figure 1: Porosity inclusion and surface roughness defects of computed tomography scan of an SLM manufactured beam on the left and the equivalent bi-material comprising interior and exterior materials on the right.

and the thickness corresponds to the mean amplitude of the surface rougness e_S [8] as shown in Figure 1 on the left .

Let us define p^k with $k \in \{int, ext\}$ the respective actual porosities of the interior and exterior materials, p_c^k with $k \in \{int, ext\}$ the respective nominal porosities of the interior and exterior materials, and $\bar{p}^k = \frac{p^k}{p_c^k}$ with $k \in \{int, ext\}$ the respective effective porosities of the interior and exterior materials. Because the two materials share the same morphology and geometry of the grain, the constant f is the same for both cases. We can write the following relation:

$$E^k = E_0(1 - \bar{p}^k)^f, \tag{2}$$

The equivalent Young's modulus of the bi-material can be written as:

$$E_{eq} = \frac{E_0}{2}\Sigma_k(1 - \bar{p}^k)^f, \tag{3}$$

The amplitude of the Young's modulus is defined as the gap between the Young's modulus of the solid material and the porous material. Thus, the amplitude can be written as follow:

$$E_a^k = a^k E_0(1 - (1 - \bar{p}^k)^f), \tag{4}$$

where a^k is the amplitude factor that indicates the Young's modulus variability intensity.

In this study, the porosity parameters will be chosen according to the reference of a sintered iron from [5] as indicated in the table below:

Table 1: Range of the porosity parameters and Young's modulus.

$E_0(GPa)$	p	p_c	f
212 ± 3.5	$0 - 0.22$	0.41 ± 0.09	1.13 ± 0.36

3 Shape and topology optimisation via level set

3.1 Shape and topology optimisation

The goal of the shape and topology optimisation is to find a shape that is a solution of a problem of the form:

$$\min_{\Omega \in \mathcal{O}_{ad}} \mathcal{J}(\Omega), \tag{5}$$

where $\mathcal{J}(\Omega)$ is a cost function that depends on the domain $\Omega \in \mathbf{R}^d$ and $\mathcal{O}_{ad}$ is the set of admissible shapes.

Relying on Hadamard's notion of shape derivative, we evaluate the cost function sensitivity with respect to a certain class of domain perturbations in order to implement an iterative continuous optimisation algorithm. A variation of a domain Ω is given by:

$$\Omega_\theta = (I + \theta)(\Omega), \tag{6}$$

where $\theta \in W^{1,\infty}(\mathbf{R}^d, \mathbf{R}^d)$ and for θ sufficiently small, $(I + \theta)$ is a diffeomorphism in $\mathbf{R}^d$.

A function $\mathcal{J}(\Omega)$ admits a shape derivative if the mapping $\theta \to \mathcal{J}(\Omega_\theta)$ from $W^{1,\infty}(\mathbf{R}^d, \mathbf{R}^d)$ to $\mathbf{R}$ is Fréchet differentiable at $\theta = 0$. The Fréchet derivative (or shape derivative) of $\mathcal{J}(\Omega)$ is denoted by $\theta \to \mathcal{J}'(\Omega)(\theta)$ and defined as:

$$\mathcal{J}(\Omega_\theta) = \mathcal{J}(\Omega) + \mathcal{J}'(\Omega)(\theta) + o(\theta), \tag{7}$$

where

$$\frac{|o(\theta)|}{||\theta||_{W^{1,\infty}(\mathbf{R}^d, \mathbf{R}^d)}} \xrightarrow{\theta \to 0} 0$$

and $\mathcal{J}'(\Omega)$ is a continuous linear form on $W^{1,\infty}(\mathbf{R}^d, \mathbf{R}^d)$.

The shape derivative depends on the normal trace of the perturbation θ in Ω [10]. In many relevant cases, it can be written as in [11]:

$$\forall \theta \in W^{1,\infty}(\mathbf{R}^d, \mathbf{R}^d), \;\; \mathcal{J}'(\Omega)(\theta) = \int_{\partial\Omega} v_\Omega(s) \theta n_\Omega \, ds, \tag{8}$$

where n_Ω is the outward unit normal to the boundary $\partial\Omega$ and $v_\Omega(s)$ depends on $\mathcal{J}(\Omega)$.

3.2 Level set method

The level set method introduced by Osher and Sethian [9] is used for the numerical implementation of the shape and topology optimisation problem. In this framework, a shape $\Omega \subset \mathbf{R}^d$ is represented by the negative subdomain of an auxiliary level set function $\phi : \mathbf{R}^d \to \mathbf{R}$:

$$\forall x \in \mathbf{R}^d, \begin{cases} \phi(x) < 0 & \text{if } x \in \Omega \\ \phi(x) = 0 & \text{if } x \in \partial\Omega \\ \phi(x) > 0 & \text{if } x \in \overline{\Omega}^c \end{cases} \tag{9}$$

The motion of a domain $\Omega(t)$ for $t \in [0, T]$ according to a normal velocity field $V(x, t)$ translates into a Hamilton-Jacobi equation for the associated level set function $\phi(t, .)$:

$$\frac{\partial \phi}{\partial t} + V|\nabla \phi| = 0, t \in (0, T), x \in \mathbf{R}^d, \tag{10}$$

where t is a pseudo-time, the upper bound T is analogous to the step size of a gradient descent and the advection field V derives from the shape derivative $\mathcal{J}'_\Omega$ of the objective function $\mathcal{J}(\Omega)$. Instead of taking the direction of steepest descent $V = -\mathcal{J}'_\Omega$, a regularisation and an extension process to compute V from $\mathcal{J}'_\Omega$ is implemented [12].

3.3 Remeshing

In this work, the strategy of domain evolution is based on the description of the level set as mentioned above and also on the explicit mesh discretisation of the level set. The level set allows abitrary shape evolutions included topology changes; on the other hand, the remeshing of the level set can describe the evolution of the form without introducing any numerical artefacts. With the exact discretisation of the level set, we can obtain the explicit mesh of the design domain $\mathcal{D}$ corresponding to the negative ϕ region [13]. After adapting the mesh to the actual level set, the mesh of the design domain D contains the computed mesh Ω as a submesh. The surface interface $\partial\Omega$ is explicitly discretised by the triangulation and the level set is reinitialised by the distance evaluation of the interface at each point of the design domain.

To obtain the topology change, the design domain is updated by equation (10). The new topology is defined implicitly by $\Omega_{k+1} = \{x \in D : \phi_{k+1}(x) < 0\}$. The explicit mesh of the design domain Ω_{k+1} is obtained by the remeshing step and the discretisation of the zero level set ϕ_{k+1} [15, 13].

This evolution strategy is used to compute the current point in the optimisation nullspace-based algorithm used in this study [14].

4 Random perturbations on materials in shape and topology optimisation

4.1 A model problem

Let us consider a linear elastic solid domain $\Omega \subset \mathbf{R}^d$. The Dirichlet boundary condition is imposed on $\Gamma_D \subset \partial\Omega$. Body and surface forces are respectively denoted by $f \in L^2(\Omega)^d$ and $g \in L^2(\Gamma_N)^d$ with $\Gamma_N \subset \partial\Omega$ and $\Gamma_0 = \partial\Omega \backslash (\Gamma_N \cup \Gamma_D)$. The mechanical problem obeys the following system of equations :

$$\left\{\begin{array}{rcccc} -\mathrm{div}(\sigma(u_\Omega)) & = & f & \text{in} & \Omega, \\ u_\Omega & = & 0 & \text{on} & \Gamma_D, \\ \sigma(u_\Omega)n & = & g & \text{on} & \Gamma_N, \\ \sigma(u_\Omega)n & = & 0 & \text{on} & \Gamma_0, \end{array}\right. \tag{11}$$

Let us define Hooke's tensor firs $A(E) \equiv E\bar{A}$ and $\sigma(u_\Omega) = Ae(u_\Omega)$, where

$$\bar{A}e = \frac{1}{2(1+\nu)}e + \frac{\nu}{(1+\nu)(1-2\nu)}tr(e)I, \forall e \in \mathcal{S}(\mathbf{R}^d), \tag{12}$$

where $\mathcal{S}$ is a regular simplex.

We introduce a small perturbation $\hat{E}$ in the equivalent Young's modulus $E = E_{eq} + \hat{E}$ such that $E_{eq} \in L^\infty(\Omega)$, and $\hat{E} = \Sigma_{i=1}^N E_{a,i}\chi_i\xi_i . E_{a,i} \in L^\infty(\Omega)$ are the amplitudes of the perturbation corresponding to the zone χ_i , N is the number of the regions and ξ_i the independent centred normal distribution.

We assume that the perturbations are random and accordingly we set $\hat{E} \equiv \hat{E}(x, \omega)$ for $x \in \Omega$ and $\omega \in \mathcal{O}$, where $(\mathcal{O}, \mathcal{F}, \mathbf{P})$ is a probability space.

The standard cost function can be written as:

$$\mathcal{M}(\Omega) = \int_{\mathcal{O}} C(\Omega, E_0 + \hat{E}(., \omega))\mathbf{P}(d\omega), \tag{13}$$

4.2 Mean of the cost function

The mean value of the second-order Taylor expansion developped in [2] can be written as:

$$\tilde{\mathcal{M}}(\Omega) = \int_\Omega X(u_\Omega, u^1_{\Omega,1}, u^1_{\Omega,2}, ..., u^1_{\Omega,N}, u^2_\Omega)dx, \tag{14}$$

where

$$X(u_\Omega, u^1_{\Omega,1}, u^1_{\Omega,2}, ..., u^1_{\Omega,N}, u^2_\Omega) = j(u_\Omega) + \frac{1}{2}\Sigma_{i=1}^N \nabla^2 j(u_\Omega)(u^1_{\Omega,i}, u^1_{\Omega,i}) + \frac{1}{2}\nabla j(u_\Omega)u^2_\Omega, \tag{15}$$

where $u^1_{\Omega,i}, i = 1...N$ are the solutions to the following equations:

$$\forall v \in H^1_{\Gamma_D}(\Omega)^d, \int_\Omega Ae(u^1_{\Omega,i}) : e(v)dx = -\int_\Omega E_i\chi_i\bar{A}e(u_\Omega) : e(v)dx, \tag{16}$$

By superimposing of the equations (16), we deduce that $u^1_\Omega = \Sigma_{i=1}^N u^1_{\Omega,i}$ is the solution to the equation:

$$\forall v \in H^1_{\Gamma_D}(\Omega)^d, \int_\Omega \sigma(u^1_\Omega) : e(v)dx = -\int_\Omega \sigma^1(u_\Omega) : e(v)dx, \tag{17}$$

where

$$\sigma^1(u_\Omega) = \Sigma_{i=1}^N \frac{E_i\chi_i}{E_{eq} + E_i\chi_i}\sigma(u_\Omega), \tag{18}$$

and u^2_Ω is the solution to the equation:

$$\forall v \in H^1_{\Gamma_D}(\Omega)^d, \int_\Omega \sigma(u^2_\Omega) : e(v)dx = -\int_\Omega \sigma^1(u_\Omega) : e(v)dx, \tag{19}$$

where

$$\sigma^2(u_\Omega) = \Sigma_{i=1}^N \frac{E_i^2\chi_i}{(E_{eq} + E_i\chi_i)^2}\sigma(u_\Omega), \tag{20}$$

4.3 Shape derivative of the mean of the cost function

According to The theorem 16 in Allaire & Dapogny [2], the Fréchet derivative of the mean of the cost function is given by :

$$\begin{array}{c}\forall \theta \in \mathcal{O}_{ad}, \tilde{\mathcal{M}}'(\Omega) = \int_\Gamma (X(u_\Omega, u^1_{\Omega,1}, u^1_{\Omega,2}, ..., u^1_{\Omega,N}, u^2_\Omega) \\ +Y(u_\Omega, p_\Omega, u^1_{\Omega,1}, p^1_{\Omega,1}, u^1_{\Omega,2}, p^1_{\Omega,2}, ..., u^1_{\Omega,N}, p^1_{\Omega,N}, u^2_\Omega, p^2_\Omega))n\theta \ ds,\end{array} \tag{21}$$

where

$$\begin{array}{l}Y(u_\Omega, p_\Omega, u^1_{\Omega,1}, p^1_{\Omega,1}, u^1_{\Omega,2}, p^1_{\Omega,2}, ..., u^1_{\Omega,N}, p^1_{\Omega,N}, u^2_\Omega, p^2_\Omega) = Ae(u^2_\Omega) : e(p_\Omega) + Ae(u_\Omega) : e(p^2_\Omega) \\ +\Sigma_{i=1}^N (E_i\chi_i \bar{A}e(u^1_{\Omega,i}) : e(p_\Omega) + Ae(u^1_{\Omega,i}) : e(p^1_{\Omega,i}) + E_i\chi_i \bar{A}e(u_\Omega) : e(p^1_{\Omega,i})),\end{array} \tag{22}$$

p_Ω is the solution of the equation:

$$\forall v \in H^1_{\Gamma_D}(\Omega)^d, \int_\Omega Ae(p_\Omega) : e(v)dx = -\int_\Omega \nabla j(u_\Omega)vdx, \tag{23}$$

$p^1_{\Omega,i}, i = 1...N$ are the solutions of the following equations:

$$\forall v \in H^1_{\Gamma_D}(\Omega)^d, \int_\Omega Ae(p^1_{\Omega,i}) : e(v)dx = -\int_\Omega \nabla^2 j(u_\Omega)(u^1_{\Omega,i}, v)dx - \int_\Omega E_i\chi_i \bar{A}e(p_\Omega) : e(v)dx, \tag{24}$$

By superimposing of the equations (24), we deduce that $p^1_\Omega = \Sigma_{i=1}^N p^1_{\Omega,i}$ is the solution to the equation:

$$\forall v \in H^1_{\Gamma_D}(\Omega)^d, \int_\Omega \sigma(p^1_\Omega) : e(v)dx = -\int_\Omega \nabla^2 j(u_\Omega)(u^1_\Omega, v)dx - \int_\Omega \sigma^1(p_\Omega) : e(v)dx, \tag{25}$$

and p^2_Ω is the solution to the equation:

$$\begin{array}{l}\forall v \in H^1_{\Gamma_D}(\Omega)^d, \int_\Omega Ae(p^2_\Omega) : e(v)dx = \\ -\int_\Omega \nabla j(u_\Omega)(u_\Omega, v)dx - \frac{1}{2}\int_\Omega \nabla^2 j(u_\Omega)(u^2_\Omega, v)dx \\ -\frac{1}{2}\int_\Omega \nabla^3 j(u_\Omega)(u^1_\Omega, u^1_\Omega, v)dx - \sigma^2(p_\Omega) : e(v)dx,\end{array} \tag{26}$$

4.4 Application to robust compliance

The so-called compliance function is defined as:

$$\mathcal{C}(\Omega) = \int_\Omega \sigma(u_\Omega) : e(u_\Omega)dx, \tag{27}$$

The approximate of the robust compliance becomes:

$$\tilde{\mathcal{M}}(\Omega) = \int_\Omega \sigma(u_\Omega) : e(u_\Omega) + \frac{1}{2}\sigma^1(u_\Omega) : e(u^1_\Omega) + \frac{1}{2}\sigma(u_\Omega) : e(u^2_\Omega)dx, \tag{28}$$

The corresponding shape derivative can be written as:

$$\forall \theta \in \mathcal{O}_{ad}, \tilde{\mathcal{M}}'(\Omega) = \int_\Gamma (\sigma(u_\Omega) : e(u_\Omega) + \frac{3}{2}(\sigma^1(u_\Omega) : e(u^1_\Omega) + \sigma(u_\Omega) : e(p_\Omega)) - \frac{1}{2}\sigma(u_\Omega) : e(u^2_\Omega))n\theta \; ds, \tag{29}$$

p_Ω is the solution of the adjoint equation:

$$\forall v \in H^1_{\Gamma_D}(\Omega)^d, \int_\Omega \sigma(p_\Omega) : e(v)dx = -\int_\Omega \sigma(u_\Omega) : e(v)dx - \int_\Omega \sigma^2(u_\Omega) : e(v)dx - \frac{1}{2}\int_\Omega \sigma(u^2_\Omega) : e(v)dx, \tag{30}$$

4.5 Evolution of amplitude zones corresponding to a topology change

As mentioned in section 2, the additively manufactured structure is divided into two zones corresponding to the porosity inclusion and the surface roughness defects. The surface roughness defect is exposed to the empty space zone. It corresponds to the level set of the designed structure. The zone of the exterior material is created by the offset of the surface of the designed structure. The offset size is equivalent to the mean amplitude of surface roughness. This value should be larger or equal to the maximum size of the mesh to be able to capture the amplitude of this zone. The zone is then updated at each iteration of the optimisation see Figure 2.

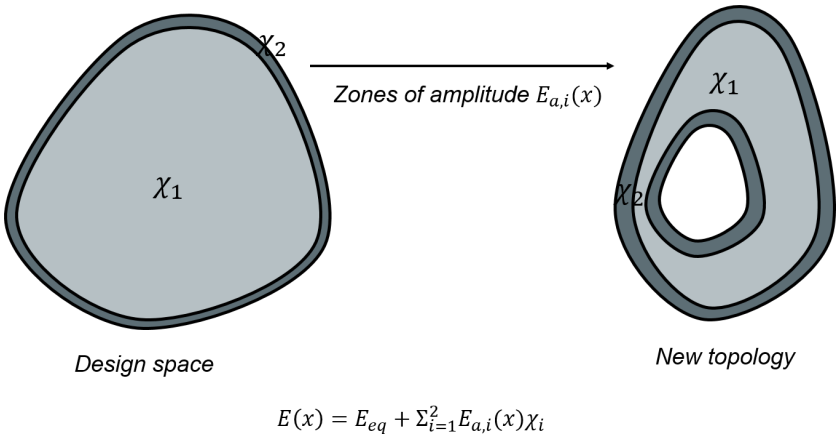

Figure 2: Evolution of amplitudes zones corresponding to the interior and the exterior materials for the design space on the left and the new topology on the right.

5 Numerical Example

In the following example, we consider the minimisation of the compliance with a $0.2m^3$ volume-constraint.

Let us consider the test case of a three-dimensional cantilever. The design domain is a box of $2m \times 0.5m \times 1m$ as shown on Figure 3 on the left. It is clamped at one extremity of the beam and a surface force is applied at another extremity $g = (-1kN, 0, 0)$. The clamped zone and the applied force zone are non-optimised zones, i.e, they are not considered in the optimisation. The nominal material parameters are $E_0 = 212GPa, \nu = 0.3$. The porous material parameters are indicated in the table below. From this table, we can compute the equivalent Young's modulus by equation (3) $E_{eq} = 141GPa$.

Figure 3 in the middle illustrates the initial design with holes. In the initial design phase, the interface offset that bounds the exterior material amplitude zone is determined as illustrated in Figure 3 on the right. The amplitude zones change at each optimisation iteration.

Table 2: Values of porosity parameters for the numerical application.

Material	p	p_c	$\bar{p}$	f
Interoir	0.08	0.41	0.2	1.13
Exteroir	0.16	0.41	0.4	1.13

The optimised shapes obtained at iteration 60 for the deterministic case and at iteration 30 for the robust case are displayed on Figure 4 and 5 on the left. This result clearly shows that the optimised solution changes significantly when uncertainties are taken into account. When the amplitudes of each material zone are introduced, the robust optimised

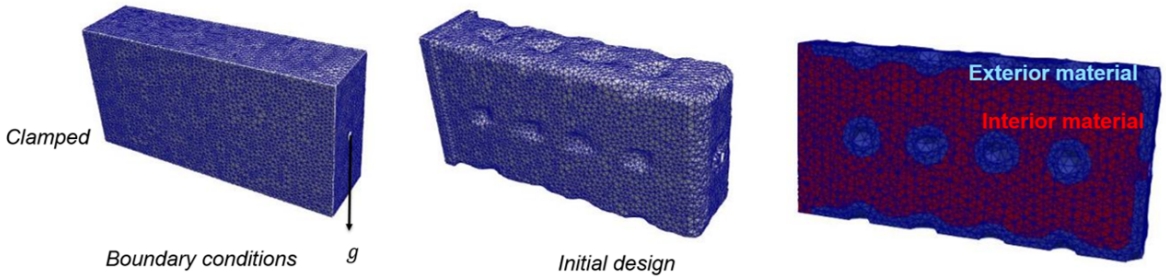

Figure 3: Boundary condition on the left, initial design in the center and the two zones of interior and exterior materials on the right.

shape exhibits a high stiffness at the high amplitude zones. The convergence histories of compliance and volume for the two cases are shown in Figure 4 and 5 on the right.

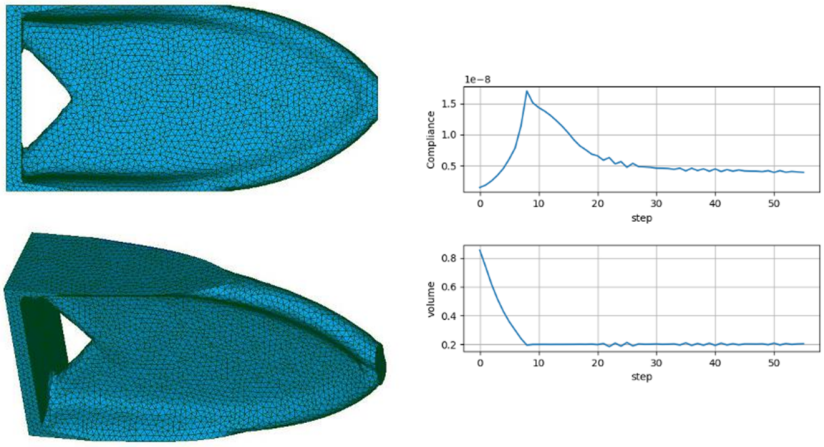

Figure 4: Final shape at iteration 60 of the deterministic optimisation on the left and the convergence history on the right.

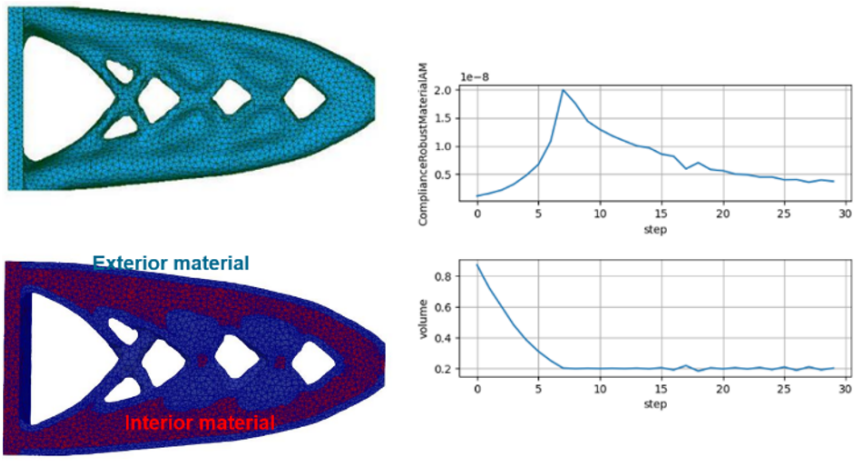

Figure 5: Final shape at iteration 30 of the robust optimisation on the left and convergence history on the right.

6 CONCLUSIONS

This paper introduces a general formulation of the deterministic formulation to take the uncertainty of the Young's modulus into account. The superimposed solutions of the adjoint equations are used to determine the approximate mean value of the cost function and the corresponding shape derivative. A strategy associating the Young's modulus value with the porosity inclusion and the surface roughness defects via two material zones (an interior and an exterior one) and an exponential law has been proposed. The numerical example of a 3D cantilever beam shows a significant change of the optimised form when uncertainties of the Young's modulus of the two zones are taken into account compared to the one obtained in the deterministic case.

REFERENCES

[1] Rodgers, T.M., Lim, H., and Brown, J.A. Three-dimensional additively manufactured microstructures and their mechanical properties. *Journal of the Minerals, Metals and Materials Society* (2020) **72**:75–82.

[2] Allaire, G. and Dapogny, C. A deterministic approximation method in shape optimization under random uncertainties. *SMAI Journal of Computational Mathematics*(2015) **1**:83–143.

[3] Dapogny, C, Dobrzynski, C., and Frey, P. Three-dimensional adaptive domain remeshing, implicit domain meshing, and applications to free and moving boundary problems. *Journal of Computational Physics* (2014) **262**:358–378.

[4] Singh, R., Gupta, A., Tripathi, O., Srivastava, S., Singh, B., Awasthi, A., Rajput, S.K. ,Sonia, P., Singhal, P., Saxena, K.K. Powder bed fusion process in additive manufacturing: An overview. *Materials Today: Proceedings*(2020)**26**:3058–3070.

[5] Kovacik, J. Correlation between Young's modulus and porosity in porous materials. *Journal of materials science letters* (1999). **18**:1007–1010.

[6] Haijun, G., K. Rafi, T. Starr and B. Stucker. The Effects of Processing Parameters on Defect Regularity in Ti-6Al-4V Parts Fabricated by Selective Laser Melting and Electron Beam Melting. *Proceedings of the Solid Freeform Fabrication Symposium*(2013).

[7] Sercombe, T., Jones, N., Day, R. et al. Heat treatment of Ti-6Al-7Nb components produced by selective laser melting. *Rapid Prototyping Journal* (2008). **14**:300–304

[8] Taufik, M., and Jain, P. K. (January 5, 2016). A Study of Build Edge Profile for Prediction of Surface Roughness in Fused Deposition Modeling. *ASME. J. Manuf. Sci. Eng.* (2016) **138(6)**: 061002.

[9] Osher, S.J. and Sethian, J.A. Front propagating with curvature-dependent speed : Algorithms based on Hamilton-Jacobi formulation.*Journal of Computational Physics* (1988) **79**:12-49.

[10] Henrot, A. and Pierre, M. Variation et optimisation de formes: une analyse géométrique. *Springer Science and Business Media* (2006) **48**.

[11] Allaire, G. Conception optimale de structures. *Springer Berlin Heidelberg New York* (2007) **58**.

[12] Allaire, G. and Jouve, F. and Toader, A.M. Structural optimization using shape sensitivity analysis and a level set method. *Journal of Computational Physics*(2004)**194(1)**:363-393.

[13] Dapogny, C. and Dobrzynski, C. and Frey, P.Three-dimensional adaptive domain remeshing, implicit domain meshing, and applications to free and moving boundary problems. *Journal of Computational Physics, Elsvier*(2014) **262**:358–378.

[14] Feppon, F. and Allaire, G. and Dapogny, C. Null space gradient flows for constrained optimization with applications to shape optimization. *ESAIM: COCV (Open Access)*(2019).

[15] Allaire, G., Dapogny, C. and Frey, P. A mesh evolution algorithm based on the level set method for geometry and topology optimization. *Structural and Multidisciplinary Optimization*(2013) **48(4)**:711–715.